Mouser and Dygert (2025)
An experimental study of clinopyroxene- and garnet-melt trace element partitioning
in Fe-rich basaltic systems
Advances in Geochemistry and Cosmochemistry 1(2): 719, https://doi.org/10.33063/agc.v1i2.719

Research article

An experimental study of clinopyroxene- and garnet-melt trace element partitioning in Fe-rich basaltic systems

Megan D. Mouser[1,2,3]✉ Nicholas Dygert[1]

[1] Department of Earth, Environmental & Planetary Sciences, University of Tennessee, Knoxville, TN, 37916, USA
[2] Earth and Planets Laboratory, Carnegie Institution for Science, Washington, D.C., 20015, USA
[3] Current Affiliation: Amentum, NASA Johnson Space Center, Astromaterials Research and Exploration Science (ARES) Division, Houston, TX, 77058, USA

✉ **Correspondence to:** M. D. Mouser: megan.d.mouser@nasa.gov

Author contributions: Conceptualization: MDM, ND; Formal analysis: MDM; Funding acquisition: ND; Investigation: MDM, ND; Methodology: MDM, ND; Visualization: MDM; Writing – original draft: MDM; Writing – review & editing: MDM, ND.

Data, code, and outputs: https://doi.org/10.5281/zenodo.16056028

Submitted: 2025-01-22
Accepted: 2025-06-30
Published: 2025-07-28

Production editor:
Ekaterina S. Kiseeva

Handling editor:
Sarah Lambart

Reviews:
J. Brian Balta,
One anonymous reviewer

Copyediting:
Marthe Klöcking

Trace elements in Fe-rich basaltic systems are important for understanding petrogenesis on the Moon and layered intrusions on Earth. To investigate crystal-chemical controls on partitioning between clinopyroxenes and garnets in Fe-rich basalts, an experimental study was conducted utilizing two synthetic compositions, a ferrobasalt (Fe-rich, Al-poor) and an intermediate basalt (relatively more Al- and Mg-rich) at approximately one log unit below the iron-wüstite buffer. Experiments were run using piston cylinder and multi-anvil apparatuses at pressures of 1 to 5 GPa, testing partitioning behavior in phases that precipitated from the endmember haplobasalts and a 50-50 mixture. We find that Al substitution into the clinopyroxene tetrahedral site influences 1+, 3+ and 4+ cation partitioning, with more aluminous samples having the highest partition coefficients for large ion lithophile elements, trivalent rare earth elements (REEs), and high field strength elements. Low-Al ferrobasalt clinopyroxenes exhibit heavy REE (HREE) partition coefficient anomalies, suggesting HREE substitution onto the M1 site, and a positive Eu partitioning anomaly. In contrast, higher-Al intermediate basalt clinopyroxenes have negative Eu partitioning anomalies and no HREE partitioning anomaly. The almandine-type garnets produced in higher-pressure experiments provide novel constraints for lunar-relevant systems. Comparison with literature data suggests these Fe-rich garnets exhibit partitioning behavior similar to garnets in more magnesian systems. Experimentally determined partition coefficients and new predictive models are applied to the petrogenesis of Fe-rich lunar basalts to evaluate their potential origins. To explain Yb/Sm ratios of black glasses, successful models invoke a minor garnet component in their mantle sources.

1 Introduction

1.1 Pyroxene and Garnet Crystal Chemistry

Trace element compositions of mafic, rock-forming minerals (e.g., olivine, orthopyroxene, clinopyroxene, garnet) are records of melting and fractionation processes during igneous petrogenesis. The distribution of incompatible trace elements among these minerals and coexisting silicate liquids is important for interpreting the significance of elemental fractionations (Sun and Liang, 2013). In particular, the rare earth element (REE) group is the most commonly applied in petrogenetic modeling (Gallahan and Nielsen, 1992). In addition to REEs, high field strength elements (HFSEs) are also useful petrogenetic indicators. Both REEs and HFSEs have high valence states (e.g., 3+, 4+) which require coupled substitution when substituting into a crystal lattice site that would typically house a 2+ cation (e.g., Mg, Fe). Experiments conducted on terrestrial Mg-rich systems found that an important coupled substitution of 3+ cations in pyroxene is substitution of Al^{3+} into the tetrahedrally coordinated site usually occupied by Si^{4+} (e.g., Colson et al., 1989; Gallahan and Nielsen, 1992; Hauri et al., 1994; Gaetani and Grove, 1995). How this dependence on Al translates to Fe-rich systems is not well understood (Dygert et al., 2014).

Among the major minerals in planetary mantles, clinopyroxenes and garnets have more favorable structures to host incompatible trace elements. Clinopyroxenes, with a general formula of $(M2)(M1)T_2O_6$, preferentially host trace elements because of the large size of the M2 site in the crystal structure. The M2 site normally houses Ca^{2+} and is large enough to accommodate substitution of cations with larger ionic radii (e.g., Cameron and Papike, 1981; Gallahan and Nielsen, 1992; Blundy and Wood, 2003; Olin and Wolff, 2010). The M1 site is less distorted (Cameron and Papike, 1981) and houses cations with smaller radii, e.g., Mg^{2+}, Fe^{2+}. Therefore, the M1 site is typically not the subject of focus when considering partitioning of elements with larger radii (e.g., REEs, HFSE), with the exception of Fe- and alkaline-rich systems where heavy REEs may partition into the M1 site in 6-fold coordination (Olin and Wolff, 2010; Dygert et al., 2014; Baudouin et al., 2020). A proposed charge-balancing coupled substitution of REE and HFSE into the M1 and M2 sites is substitution of Al^{3+} in the tetrahedral site, but there can be other coupled substitution mechanisms such as jadeite component or vacancy substitution.

The garnet crystal structure ($X_3Y_2Si_3O_{12}$) has an "X" site, which generally hosts Ca^{2+}, Mg^{2+}, and Fe^{2+}, however, this site can also incorporate incompatible trace elements due to the larger size of cations that normally occupy the site, much like clinopyroxenes (Novak and Gibbs, 1971; van Westrenen et al., 2001). The garnet trace element signature is characteristic in its preference for heavy REEs (HREEs), with concentrations up to several orders of magnitude greater than light REEs (LREEs) in natural garnets in igneous and metamorphic systems (e.g., Sun and Liang, 2013; Tual et al., 2022; Blatter et al., 2023).

Clinopyroxene- and garnet-melt trace element partitioning studies have mainly focused on Mg-rich basaltic systems (e.g., Yurimoto and Ohtani, 1992; Gaetani and Grove, 1995; Johnson, 1998; Salters and Longhi, 1999; van Westrenen et al., 1999; Sun and Liang, 2012; Bédard, 2014; Sun et al., 2017). These studies found the main controls on trace element partitioning are the compositions of the mineral and melt, oxygen fugacity (fO_2), and pressure and temperature. Melt polymerization may strongly affect clinopyroxene-melt partition coefficients in silicic systems (Olin and Wolff, 2010), but in basaltic systems, melt structure appears to play a subordinate role to crystal chemistry, at least for the REEs (e.g., Sun and Liang, 2012).

In Fe-rich systems, clinopyroxene composition affects partitioning of heavy REEs (Olin and Wolff, 2010; Dygert et al., 2014), where in 6-fold coordination in the M1 site has been noted. This behavior could be attributed to the similar ionic radii between HREE in 6-fold coordination and Fe^{2+} (e.g., Lu in 6-fold-0.861 Å vs. 8-fold-0.977 Å, and Fe^{2+} in 6-fold-0.780 Å, Shannon, 1976). Existing predictive models for clinopyroxene-melt trace element partitioning (Sun and Liang, 2012; Dygert et al., 2014, 2015) are not suited to model the HREE partitioning onto the M1 lattice site. The nature of charge balancing coupled substitutions in Fe-rich systems is also uncertain (Dygert et al., 2014). Evaluating the influence of pyroxene Fe and Al content on trace element partitioning behavior requires new constraints from experiments conducted in ferrobasaltic systems, which are presented in this work.

1.2 The Importance of Fe-rich Minerals in Lunar Petrogenesis

Experimental compositions presented in this work are analogous to the lunar magma ocean and thus the trace element partitioning data from the experiments are ultimately applied to the petrogenesis of lunar basalts (see Section 4.5). Here we provide general lunar context for the partitioning data. Lunar basalts range in composition, e.g., in their Fe and Ti contents, which vary up to 24 wt% in FeO and <1 to 14 wt% TiO_2 (e.g., Papike et al., 1976; Neal and Taylor, 1992), with fO_2s estimated to be ~IW-1 (e.g., Wadhwa, 2008). The compositional diversity reflects the differentiation history of the Moon. Geophysical and petrological constraints from sample analysis suggest that the Moon's mantle formed distinct layers during magma ocean solidification (Ohtani, 1985; Warren, 1985; Snyder et al., 1992). One such layer represents the end of the magma ocean solidification (~95–99% crystallization; Shearer and Papike, 1999) and precipitated from a residual liquid highly enriched in incompatible elements such as potassium, REE, phosphorous, uranium, and thorium (referred to as urKREEP; Warren, 1985). Evidence for this layer, which would have comprised dense ilmenite and Fe-rich clinopyroxene cumulates, is exhibited in the enrichment of Ti and a KREEPy trace element signature in lunar basalt samples (e.g., Walker et al., 1975; Hess et al., 1978; Snyder et al., 1992). The KREEPy ilmenite and clinopyroxene-rich late magma ocean cumulates would have been much denser than the underlying cumulates, resulting in a gravitationally unstable density stratification, causing gravitational instabilities to form and sink into the interior (e.g., Kesson and Ringwood, 1976; Hess and Parmentier, 1995; Zhang et al., 2017; Li et al., 2019; Yu et al., 2019). This process would have mixed the dense ilmenite and KREEP-bearing material with the underlying mafic cumulates forming Ti- and KREEP-rich hybridized mantle source regions capable of producing the compositional diversity of lunar basalts found on the surface of the Moon today.

Lunar basalts and glasses sourced from the Moon's interior and are broadly divided into categories based on their Ti content (very low-Ti, low-Ti, and high-Ti). Lunar glasses are referred to by color which is a proxy for Ti abundance (with increasing Ti, green, yellow, orange, black) (Shearer et al., 1991; Shearer and Papike, 1993). In addition to the wide range of Ti and REE abundances exhibited by these basalts, there is also variation in their Hf and Nd isotopic compositions (e.g., Unruh et al., 1984; Beard et al., 1998; Münker, 2010) which suggests mixing of distinct magma ocean cumulates in their mantle sources (hybridization), facilitated by cumulate mantle overturn.

The deep lunar mantle is thought to consist of olivine, orthopyroxene, and clinopyroxene (e.g., Snyder et al., 1992). However, garnet has been proposed to exist in the deep lunar mantle due to the ratios of HFSE in lunar samples, predictions of the lunar mantle mineralogy from fractional crystallization models, and experimental investigations of the sound velocities of the lunar mantle (Beard et al., 1998; Neal, 2001; Draper et al., 2006; Barr and Grove,

Table 1. Major element experimental compositions.

	SiO_2	TiO_2	Al_2O_3	MgO	CaO	MnO	FeO	Na_2O	K_2O	P_2O_5	Dopant	Total
Intermediate Basalt	35.85	2.72	5.04	2.69	10.35	0.63	39.44	0.16	0.28	0.53	0.34	98.03
1σ StDev	0.24	0.04	0.39	0.03	0.07	0.07	0.19	0.02	0.01	0.02	0.02	
Ferrobasalt	34.58	3.68	0.49	1.01	10.70	1.10	44.57	0.10	0.16	0.48	0.33	97.20
1σ StDev	0.57	0.11	0.01	0.03	0.22	0.03	1.04	0.01	0.01	0.01	0.02	
FR1290a	44.16	4.05	8.67	0.26	10.89	0.70	29.86	0.50	0.36	0.40		99.85

Table 2. Experimental run conditions and phases for all experiments. Pyx = pyroxene, Gt = garnet, Ilm = ilmenite, Ol = olivine.

Experiment	Composition	Pressure (GPa)	Superliquidus Temperature (°C)	Dwell Temperature (°C)	Dwell Period (h)	Phases
FR1290-Hd-1	Ferrobasalt	1	1,300	1,120	48	Pyx + Fe Metal + Glass
FR1290-Aug-2	Intermediate Basalt	1	1,300	1,150	56	Pyx + Glass
FR1290-5050HdAug-1	50-50 Mix	1	1,300	1,150	51	Pyx + Fe Metal + Glass
FR1290-Hd-3	Ferrobasalt	2	1,350	1,175	59	Pyx + Fe Metal + Glass
FR1290-Aug-3	Intermediate Basalt	2	1,350	1,175	48	Pyx + Gt + Fe Metal + Glass
FR1290-5050HdAug-2	50-50 Mix	2	1,350	1,175	58	Pyx + Fe Metal + Glass
FR1290-Aug-4	Intermediate Basalt	3	1,390	1,190	45	Pyx + Gt + Ilm + Fe Metal + Glass
FR1290-Aug-5	Intermediate Basalt	5	1,445	1,245	43	Pyx + Gt + Ol + Fe Metal + Glass

2013; Jing et al., 2022; Wood et al., 2024). Thus, garnet may be an important mineral to consider for deep magma genesis on the Moon and is tested, along with other lunar relevant minerals (olivine, orthopyroxene, clinopyroxene), in the applications of this work.

2 Methods

2.1 Compositions

A composition based on a late lunar magma ocean residual liquid analogue (FR-1290) from Longhi (2003) was used to prepare two endmember basalt compositions to explore the effects of Al and Fe on partitioning in Fe-rich systems. One has no added Al and a higher Fe content (ferrobasalt), while the other has a more moderate Fe content and higher Al (Mg# of approximately 50, where Mg# is defined as 100×Mg/(Mg+Fe), in moles) representing an intermediate basalt. These mixtures were made from reagent grade oxide and carbonate powders ground in an agate mortar and pestle for 6 hours. Both compositions were spiked with a REE/HFSE/alkali earth element mixture of ~0.3 wt% of the total composition. After the grinding and doping process, the compositions were decarbonated at 900 °C for 24 hours in an alumina crucible. After decarbonation the powders were conditioned to one log unit below the iron-wüstite (IW) buffer at 800 °C using H_2/CO_2 mixture (Deines et al., 1974, 1976) in a 1-bar horizontal gas mixing furnace at Brown University. Major element compositions of glassed samples of both compositions are presented in Table 1. For a list of analyzed trace elements, see Table S2 in the data and software publication for this work (Mouser, 2025).

2.2 Experimental Techniques

Experiments were conducted at 1 to 2.5 GPa in 150-ton end-loaded piston cylinder (PC) apparatuses at the University of Tennessee (UT) and Boyd-England style PC at the Earth and Planets Laboratory (EPL), Carnegie Institution for Science in graphite lined Mo (UT) or Pt (EPL) capsules. Assemblies used NaCl (UT) or Talc cells (EPL) as a confining medium and were placed in 3/4" pressure vessels (1/2" for 2.5 GPa) and pressurized before heating. A 5 GPa experiment was conducted in a 1500-ton Walker-type multi-anvil apparatus at EPL in an 18/11 MgO cast octahedra (Bertka and Fei, 1997) in a graphite lined Pt capsule. The programs set for each experiment were a rapid ramp to superliquidus temperature (1300–1445 °C) at a rate of 70 °C/min, dwell for 1 hour, a slow cool to final temperature (1120–1245 °C) at a rate of 0.1 °C/min, and dwelling at the target temperature for at least 43 hours before an isobaric quench (Table 2). The range of superliquidus and final dwell temperatures were selected to produce appropriate proportions of crystals and glass, with the more magnesian experiments requiring higher temperatures than the ferrobasalt. Initial superliquidus temperature estimates at 1 GPa were based on experiments testing the base FR-1290 composition from Longhi (2003) and confirmed with a glass experiment for each composition.

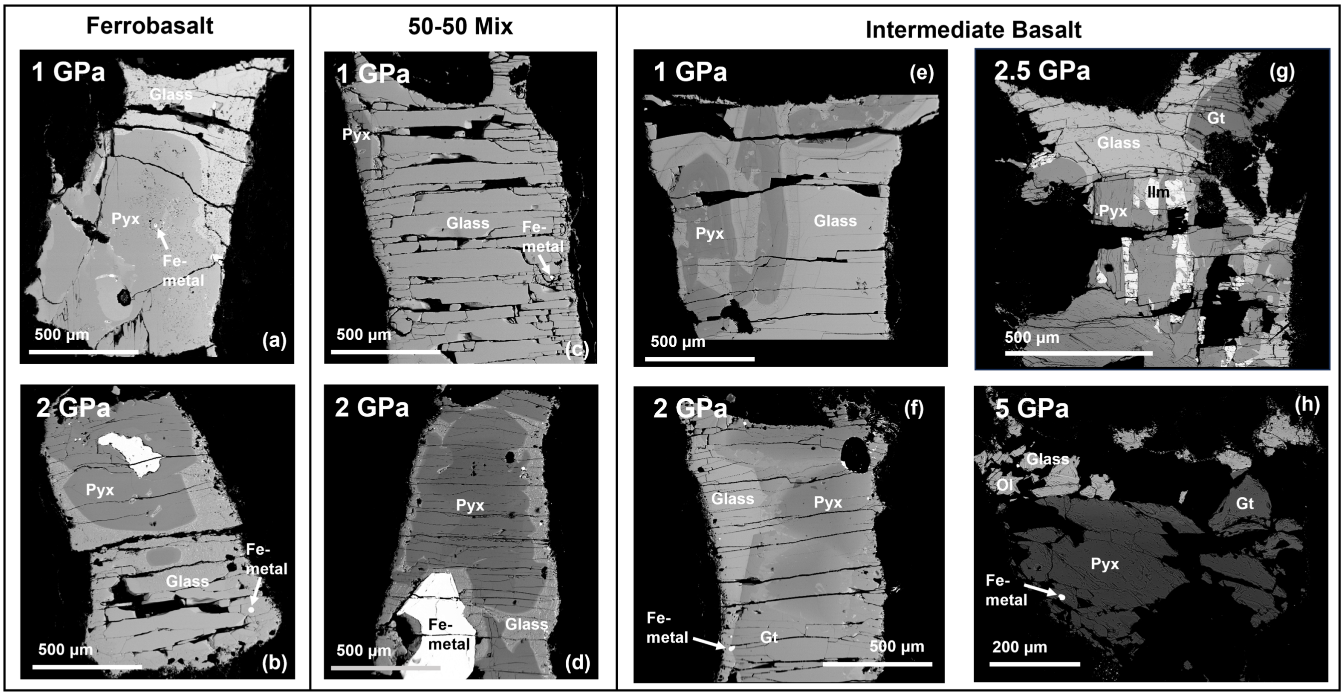

Figure 1. Representative backscattered electron micrographs of recovered experiments of ferrobasalt (a-b) and 50-50 mix (c-d) compositions at 1 and 2 GPa and intermediate basalt composition (e-h) at 1–5 GPa. Pyx = Pyroxene, Gt = Garnet, Ilm = Ilmenite, Ol = Olivine.

2.3 Electron Microprobe Analysis

After the experiments were quenched, they were mounted in epoxy and polished for electron probe micro analysis (EPMA). Analyses were conducted using a Cameca SX100 instrument at UT and JEOL JXA-8530F instrument at EPL. Major elements were analyzed at an accelerating voltage of 15 kV, a beam current of 20 nA, and a 2 µm spot size. Backscattered electron images of each experimental charge are shown in Figure 1.

2.4 Laser Ablation Inductively Coupled Plasma Mass Spectrometry

Trace element data were collected by laser ablation inductively coupled plasma mass spectrometry (LA-ICP-MS) at the University of Texas at Austin on the recovered experimental glasses and crystal rims. Spot sizes were 50 µm for all experiments except for the 5 GPa experiment which used 30 µm spot size due to the smaller sample size. Data were collected with a laser fluence of 2.03 J/cm^3 at 20 Hz with a 60 second dwell and 30 second gas blank. The reference materials were NIST612 and NIST610 used as primary standards, and NIST610, NIST612, BHVO2G, and BCR-2G used as secondary standards. Reflected light images of each experiment with LA-ICP-MS analysis pits are included in the Supplementary Material (Figures S1 and S2).

3 Results

3.1 Major Element Chemistry

Major element chemistry of the pyroxenes range from near endmember hedenbergite in the ferrobasalt experiments to augite in the intermediate basalt experiment (Table 3, Figure 2). Here, the rim compositions of the pyroxenes were used for analysis as they represent the closest approach to equilibrium with the coexisting melt. Measured glass compositions are homogeneous across each sample (bulk analyses reported in Table S1, Mouser, 2025). Intermediate basalt experiments at 2 GPa and above produced garnet in addition to pyroxene, with a resulting composition that is more Fe-rich than previously reported garnet compositions in trace element partitioning studies, plotting toward the almandine (Alm) component of the pyrope-grossular-almandine ternary (Figure 2b). Major element data for ilmenite and olivine produced in the 2.5 and 5 GPa experiments are published in Mouser (2025, Table S1).

3.2 Trace Element Chemistry and Partition Coefficients

Trace element abundances (in ppm) in glass, garnet, and pyroxene are presented in Mouser (2025, Table S2). Elemental concentrations were used to calculate the experimentally determined partition coefficients ($D^i_{crystal-melt}$) for each element:

$$D^i_{crystal-melt} = \frac{C^i_{crystal}}{C^i_{melt}} \quad (1)$$

where $C^i_{crystal}$ is the element concentration in the crystal (garnet or clinopyroxene), C^i_{melt} is the element concentration in the liquid, and i refers to the element. The partition coefficients are reported in Table 4.

Table 3. Pyroxene, garnet, and glass major element composition. Averaged major element chemistry (wt% oxide) of pyroxene rims, garnet, and glass for each experiment.

	SiO_2	TiO_2	Al_2O_3	Cr_2O_3	MgO	CaO	MnO	FeO	Na_2O	K_2O	P_2O_5	Dopant	Total
Pyroxene Rims (wt% oxide)													
Intermediate Basalt (1 GPa) n= 4	49.61	0.79	1.70	0.00	9.90	18.70	0.52	18.56	0.04			0.04	99.86
1σ StDev	0.44	0.08	0.26	0.00	0.66	0.24	0.02	1.15	0.01			0.00	
50-50 Mix (1 GPa) n= 6	48.01	0.91	0.81	0.01	4.79	18.10	0.93	26.18	0.04			0.03	99.81
1σ StDev	0.21	0.05	0.09	0.01	0.32	0.21	0.02	0.62	0.01			0.00	
50-50 Mix (2 GPa) n= 20	47.77	0.87	1.43	0.01	4.06	16.63	0.92	27.78	0.14			0.04	99.65
1σ StDev	0.36	0.08	0.21	0.01	0.53	0.51	0.04	1.02	0.02			0.00	
Ferrobasalt (1 GPa) n= 3	47.54	0.96	0.07	0.00	1.83	16.51	1.42	31.85	0.03			0.02	100.23
1σ StDev	0.37	0.11	0.01	0.00	0.70	1.53	0.11	2.29	0.00			0.00	
Ferrobasalt (2 GPa) n= 34	47.85	1.08	0.19	0.01	2.73	17.33	1.09	29.28	0.33			0.06	99.95
1σ StDev	0.72	0.34	0.08	0.01	0.50	1.32	0.13	1.83	0.05			0.01	
Garnet (wt% oxide)													
Intermediate Basalt (2 GPa) n= 8	36.05	3.00	18.87	0.01	1.04	9.09	1.21	30.79	0.02		0.04	0.39	100.50
1σ StDev	0.12	0.40	0.29	0.01	0.03	0.25	0.04	0.12	0.01		0.01	0.05	
Intermediate Basalt (2.5 GPa) n= 31	36.50	2.24	19.32	0.00	0.87	8.58	0.89	31.80	0.03		0.10	0.40	100.69
1σ StDev	0.22	0.37	0.30	0.00	0.50	0.42	0.07	1.21	0.10		0.03	0.05	
Intermediate Basalt (5 GPa) n= 13	38.54	1.75	20.61	0.00	7.24	9.51	0.93	21.71	0.01		0.10	0.88	101.28
1σ StDev	0.14	0.25	0.24	0.00	0.31	0.30	0.03	0.56	0.01		0.03	0.09	
Glass (wt% oxide)													
Intermediate Basalt (1 GPa) n= 8	42.55	3.96	7.75	0.01	2.41	11.06	0.68	28.81	0.21	0.38	0.76	0.63	99.21
1σ StDev	0.75	0.09	0.07	0.01	0.13	0.13	0.01	0.55	0.02	0.01	0.05	0.04	
Intermediate Basalt (2 GPa) n= 15	38.28	6.77	6.11	0.00	0.55	8.27	0.56	34.71	0.31	0.85	0.76	1.16	98.32
1σ StDev	0.64	0.29	0.30	0.00	0.02	0.06	0.01	0.22	0.02	0.02	0.06	0.08	
Intermediate Basalt (2.5 GPa) n= 9	31.74	6.48	3.03	0.00	0.22	6.80	0.41	39.73	0.30	2.41	4.38	2.99	98.49
1σ StDev	0.45	0.12	0.09	0.00	0.01	0.08	0.02	0.26	0.02	0.05	0.31	0.02	
Intermediate Basalt (5 GPa) n= 17	29.25	7.96	3.43	0.00	2.63	8.22	0.59	43.60	0.41	0.74	1.54	1.31	99.67
1σ StDev	0.79	0.97	0.20	0.00	0.40	0.55	0.05	1.05	0.09	0.32	0.27	0.08	
50-50 Mix (1 GPa) n= 7	41.01	4.87	4.18	0.00	1.11	10.81	1.10	33.65	0.23	0.26	0.75	0.66	98.63
1σ StDev	0.66	0.06	0.03	0.00	0.02	0.05	0.02	0.50	0.02	0.01	0.04	0.04	
50-50 Mix (2 GPa) n= 4	36.62	7.89	3.82	0.01	1.06	9.30	1.08	39.73	0.17	0.04	0.44	0.65	100.38
1σ StDev	4.89	3.52	1.42	0.01	0.38	2.09	0.20	5.05	0.04	0.07	0.02	0.04	
Ferrobasalt (1 GPa) n= 4	35.83	8.32	0.47	0.00	0.30	9.11	1.59	40.95	0.20	0.12	0.99	1.14	99.02
1σ StDev	0.23	0.59	0.04	0.00	0.02	0.21	0.02	0.57	0.03	0.07	0.16	0.07	
Ferrobasalt (2 GPa) n= 15	34.53	6.26	0.46	0.00	0.77	9.41	1.42	43.20	1.14	0.10	0.63	0.84	98.79
1σ StDev	1.19	0.80	0.04	0.00	0.11	0.72	0.72	1.64	0.25	0.08	0.07	0.06	

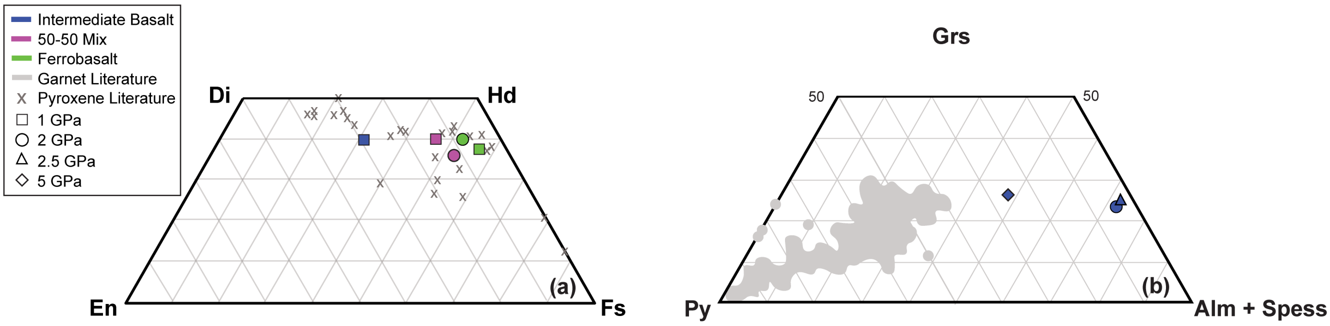

Figure 2. (a) Average pyroxene rim composition for each experiment; Di = diopside ($CaMg(Si,Al)_2O_6$), Hd = hedenbergite ($CaFe(Si,Al)_2O_6$), En = enstatite ($MgSiO_3$), Fs = ferrosilite ($FeSiO_3$). (b) Average garnet composition from the 2 GPa intermediate basalt experiment; Grs = grossular ($Ca_3Al_2(SiO_4)_3$, Py = pyrope ($Mg_3Al_2(SiO_4)_3$), Alm = almandine ($Fe_3Al_2(SiO_4)_3$), Spess = spessartine ($Mn_3Al_2(SiO_4)_3$). Literature compositions for Fe-rich and intermediate clinopyroxene-melt experiments from Pertermann and Hirschmann (2002); Olin and Wolff (2010); Dygert et al. (2014); Beard et al. (2019); Snape et al. (2022). Published garnet compositions from garnet-melt experiments: Yurimoto and Ohtani (1992); Johnson (1998); Salters and Longhi (1999); van Westrenen et al. (1999, 2000); Klemme et al. (2002); Salters et al. (2002); Bennett et al. (2004); Corgne and Wood (2004); Pertermann et al. (2004); Walter et al. (2004); Draper et al. (2006); Dwarzski et al. (2006); Tuff and Gibson (2007); Corgne et al. (2012); Suzuki et al. (2012).

Among the pyroxenes, the 1 GPa Al-poor ferrobasalt sample exhibited the lowest REE partition coefficients, whereas the 1 GPa Al-rich intermediate basalt and 2 GPa ferrobasalt samples have the highest REE partition coefficients (Figure 3; see Section 4.2 for interpretation). Pyroxenes produced in high pressure intermediate basalt experiments that also grew garnet are not included in the formal analysis. They exhibit partition coefficient variations diverging from the other experimental results, specifically, steep linear variations in partition coefficient with ionic radius and lack of parabolic curvature with ionic radius. We speculate that these features may be kinetic artifacts produced by concomitant growth of pyroxene and garnet or may be a result of mixed analysis due to the mantling of garnet around the pyroxene. According to visual inspection (see BSE images, Figure 1), and time-signal data from LA-ICP-MS analyses, garnets in these experiments do not appear to be similarly affected. The garnet experiments exhibit a general trend of increasing in REE partition coefficient with increasing experimental pressure and temperature (Figure 3c-d).

The REE partition coefficients for the experimental pyroxene rims (Figure 3a) systematically increase with increasing Al content as demonstrated by the 1 GPa experimental series. All experimental pyroxenes exhibit lower LREE than HREE partition coefficients. A feature of note is the Eu partitioning anomalies. Eu partitioning anomalies are commonly observed in systems where the redox sensitive Eu is dominantly in 2+ oxidation state while the other REEs are 3+, causing Eu to partition differently than neighboring elements with similar atomic number due to its different radius and valence state (e.g., Drake, 1975). The intermediate basalt exhibits a negative Eu partitioning anomaly while the 1 GPa ferrobasalt, and to a lesser extent the 1 and 2 GPa 50-50 mix and 2 GPa ferrobasalt, show positive Eu partitioning anomalies. This is striking as the experimental assembly and starting material preconditioning procedure produces an fO_2 about a log unit below the IW buffer, as determined from Pt-Fe alloying in included sensors (Medard et al., 2008; Ji and Dygert, 2024) and the presence of Fe-metal blebs in most experiments (Figure 1), such that the experiments were conducted at consistent fO_2s relative to the buffer. A second feature of note is the HREE partitioning anomalies in the ferrobasaltic pyroxenes. In the ferrobasalt (and 50-50 mix), there is a significant increase in HREE partition coefficients Yb and Lu not exhibited by pyroxene in the intermediate basalt which has a consistent partition coefficients across the HREEs (Figure 3a).

The clinopyroxene-melt partition coefficients for other trace elements (large ion lithophile elements, LILE, high field strength elements, HFSE, transition metals, and U and Th) are presented in the Supplementary Material, Figure S3. The HFSE partition coefficients mimic the trends exhibited by the REEs in pyroxenes with more aluminous compositions (intermediate basalt for 1 GPa and 50-50 mix for 2 GPa) having higher partition coefficients than the Al-poor ferrobasalt. U and Th show similar sensitivity to composition, both being measurable in the aluminous intermediate basalt, and both below detection limit in the Al-free 1 GPa ferrobasalt. The 1 and 2 GPa 50-50 mix and 2 GPa ferrobasalt contain measurable amounts of Th only (Figure S3).

Garnet partition coefficients for REEs are similar to what has been observed in previous studies (Figure 3c). The partition coefficients are low for LREEs and >1 for HREEs. Among LILEs, HFSEs, transition metals, and U and Th, all experimental garnet partition coefficients nearly overlap among experiments (Figure S4).

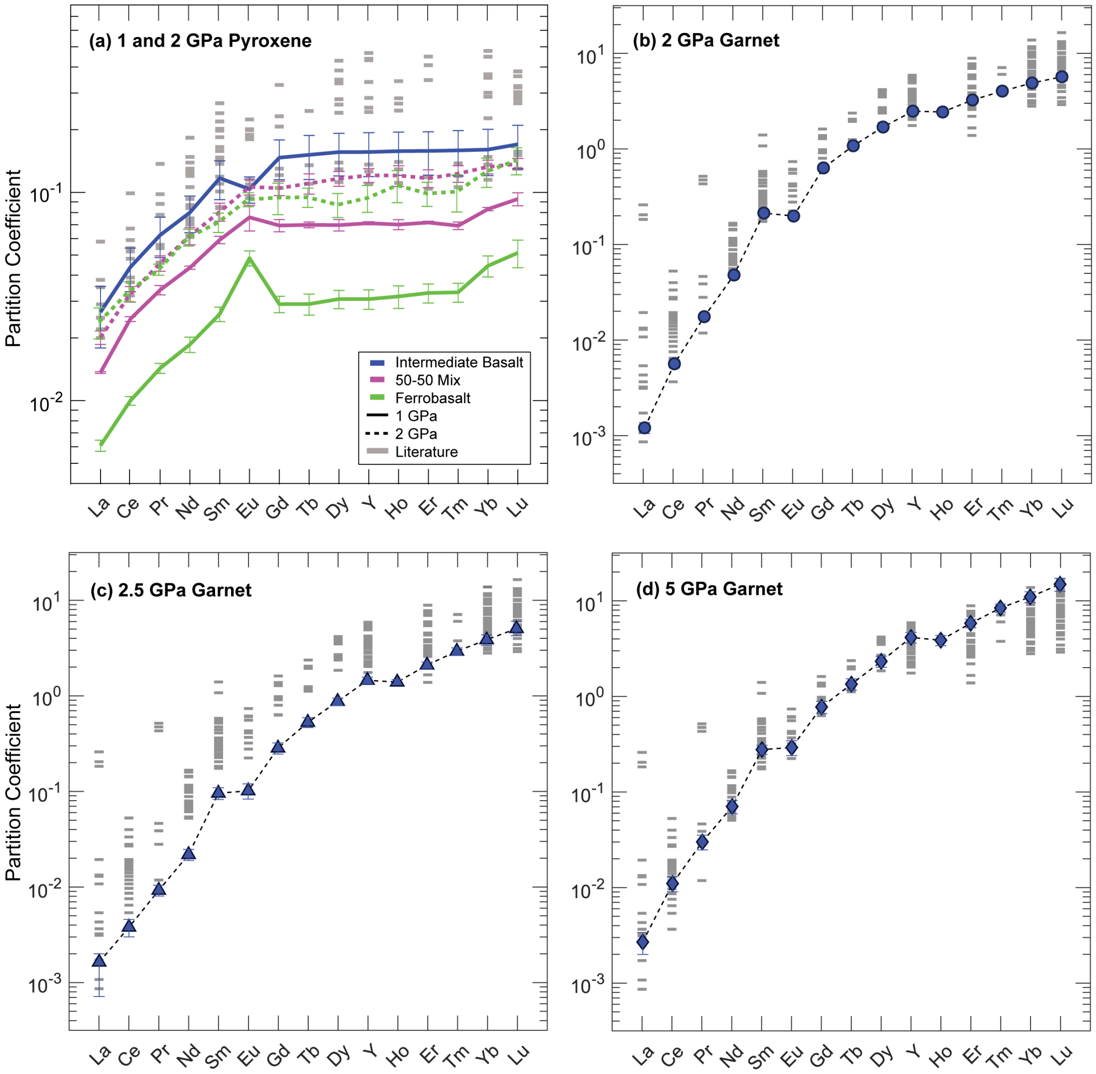

Figure 3. REE partition coefficients for 1 and 2 GPa pyroxene rims calculated using Equation 1 for (a) experiments and relevant clinopyroxene partition coefficients from literature (Pertermann and Hirschmann, 2002; Dygert et al., 2014; Snape et al., 2022), and (b-d) experimental garnet partition coefficients and partition coefficients from literature in gray (Johnson, 1998; Salters and Longhi, 1999; Klemme et al., 2002; Salters et al., 2002; Bennett et al., 2004; Pertermann et al., 2004; van Westrenen et al., 1999, 2000).

4 Discussion

4.1 Partition Coefficient Variation with Ionic Radius

The lattice strain model enables prediction of a partition coefficient for a cation of a given size and charge substituting into a specific lattice site if the properties of the site are known (e.g., Blundy and Wood, 2003). The lattice strain model is defined by the Brice equation (Brice, 1975):

$$D_i = D_0 \times \\ exp\left(\frac{-4\pi E N_A \left(\frac{r_0}{2}\right)(r_0 - r_i)^2 - \left(\frac{1}{3}\right)(r_0 - r_i)^3}{RT}\right) \quad (2)$$

where D_0 is the ideal Nernst partition coefficient for strain free substitution into the lattice site (Eq. 1), E is the effective Young's modulus of the site, N_A is Avogadro's number, r_i is the cation radius, r_0 is the crystal site radius, R is the gas constant, and T is the temperature in K. The lattice strain model is used to define parabola(s) for partitioning of isovalent cations into a specific site as a function of their ionic radii. This model has been instrumental in interpreting controls on trace element partitioning behavior.

The elements in this study were grouped by valence state and probable substitution sites, M1 or M2 in clinopyroxene and X in garnet, according to their ionic radii (Shannon, 1976) and their observed partitioning behavior. Nonlinear regressions were used to calculate D_0, E, r_0 for the lattice strain equation (Eq. 2) from each experimental data set with enough observations (three or more elements). For clinopyroxenes, lattice strain parameters are reported in Table 4 and the model fits are plotted with the experimental determinations in Figure 4. The fit quality was tested by comparing the modeled partition coefficients to the measured partition coefficients (Figure S6). Model predictions for Ba fall off parabolas defined by other divalent elements in pyroxenes; however, Ba concentrations are near LA-ICP-MS detection limit (~0.01 ppm) and the partition coefficients

Table 4. Calculated pyroxene and garnet partition coefficients.

	Pyroxene									
	Ferrobasalt 1 GPa	Uncertainty	Ferrobasalt 2 GPa	Uncertainty	50-50 Mix 1 GPa	Uncertainty	50-50 Mix 2 GPa	Uncertainty	Intermediate Basalt 1 GPa	Uncertainty
Li	0.202	0.037	0.132	0.037	0.217	0.074	0.334	0.049	0.37	0.081
Sc	1.129	0.065	1.441	0.18	1.135	0.087	1.328	0.071	1.134	0.072
Ba	0.000 35	0.0006	0.0006	0.000 04	0.000 26	0.000 07	0.0015	0.0013	0.0049	0.011
V	2.261	0.227	2.371	0.25	3.406	0.153	2.724	0.291	5.703	0.624
Zn	0.247	0.043	0.219	0.069	0.327	0.034	0.484	0.125	0.383	0.073
Sr	0.092	0.007	0.175	0.009	0.101	0.001	0.164	0.013	0.093	0.005
Y	0.031	0.003	0.093	0.014	0.071	0.001	0.117	0.013	0.156	0.037
Zr	0.003	0.0004	0.0079	0.003	0.011	0.002	0.021	0.002	0.042	0.018
Nb	0.000 18	0.000 07	0.000 45	0.000 12	0.000 51	0.000 11	0.000 56	0.000 11	0.005	0.0095
Mo	0.225	0.122	0.205	0.027	0.89	0.348	0.13	0.098	0.559	1.803
La	0.0061	0.0004	0.024	0.004	0.014	0.0001	0.019	0.002	0.027	0.009
Ce	0.01	0.0005	0.033	0.004	0.025	0.001	0.032	0.004	0.044	0.01
Pr	0.014	0.001	0.042	0.003	0.034	0.002	0.045	0.005	0.062	0.014
Nd	0.019	0.002	0.06	0.006	0.043	0.001	0.06	0.007	0.08	0.016
Sm	0.026	0.002	0.071	0.008	0.059	0.002	0.08	0.008	0.117	0.025
Eu	0.048	0.004	0.092	0.007	0.076	0.011	0.102	0.009	0.104	0.015
Gd	0.029 06	0.0026	0.094	0.016	0.069	0.005	0.1016	0.012	0.147	0.032
Tb	0.0291	0.0034	0.094	0.01	0.0698	0.002	0.107	0.017	0.151	0.036
Dy	0.031	0.003	0.086	0.011	0.0696	0.004	0.113	0.012	0.156	0.036
Ho	0.032	0.004	0.107	0.019	0.07	0.004	0.118	0.013	0.1577	0.037
Er	0.0329	0.003	0.098	0.013	0.072	0.001	0.113	0.015	0.1582	0.037
Tm	0.0331	0.003	0.1	0.02	0.069	0.003	0.119	0.015	0.159	0.039
Yb	0.044	0.005	0.125	0.02	0.083	0.002	0.129	0.015	0.161	0.04
Lu	0.051	0.008	0.141	0.021	0.093	0.007	0.133	0.013	0.17	0.04
Hf	0.0065						0.061	0.012	0.084	0.033
Ta	0.000 082	0.000 024	0.000 17	0.000 06	0.000 43	0.000 11	0.000 56	0.000 11	0.006	0.0096
W									0.014	0.009
Th			0.0005		0.000 45	0.0001	0.000 74	0.0002	0.0053	0.0098
U									0.017	0.019

Table 4. Continued.

	Garnet					
	Intermediate Basalt 2 GPa	Uncertainty	Intermediate Basalt 2.5 GPa	Uncertainty	Intermediate Basalt 5 GPa	Uncertainty
Li	0.144	0.024	0.191	0.046		
Sc	0.975	0.045	1.036	0.058	1.512	0.087
Ba			0.0012	0.0009		
V	7.19	0.65	18.12	7.335	7.113	0.555
Zn	0.258	0.025	0.171	0.04	0.166	0.037
Sr	0.0013	0.0001	0.0019	0.0008	0.0022	0.0002
Y	2.445	0.093	1.474	0.114	4.224	0.54
Zr	0.104	0.013	0.045	0.005	0.194	0.031
Nb	0.0017	0.0003	0.0018	0.0008	0.0028	0.0006
Mo	6.557	6.683	0.589	0.614		
La	0.0012	0.000 15	0.0016	0.0009	0.0027	0.0007
Ce	0.0055	0.0005	0.0038	0.0008	0.011	0.002
Pr	0.017	0.001	0.009	0.001	0.03	0.005
Nd	0.047	0.004	0.022	0.003	0.071	0.012
Sm	0.209	0.015	0.096	0.014	0.282	0.031
Eu	0.194	0.015	0.102	0.019	0.296	0.053
Gd	0.621	0.033	0.287	0.038	0.787	0.114
Tb	1.06	0.044	0.534	0.063	1.367	0.188
Dy	1.667	0.07	0.884	0.075	2.369	0.317
Ho	2.397	0.085	1.411	0.088	3.945	0.485
Er	3.203	0.173	2.129	0.16	5.941	0.607
Tm	3.968	0.262	2.972	0.261	8.587	0.849
Yb	4.826	0.281	3.923	0.495	11.231	1.489
Lu	5.609	0.525	5.135	0.807	15.236	2.373
Hf	0.18	0.025	0.056	0.008	0.206	0.034
Ta	0.0032	0.0007	0.0028	0.001	0.0049	0.0013
W	0.038	0.002	0.0046	0.0028	0.0011	0.0004
Th	0.001	0.0001	0.0017	0.001	0.0043	0.001
U	0.007	0.0007	0.0037	0.0012	0.015	0.002

exhibit considerable uncertainty (Figures 5 and S6). Lu and Yb are assumed to substitute onto the M1 site in 6-fold coordination for the ferrobasalt and 50-50 mix, and in 8-fold coordination for M2 in the intermediate basalt.

The lattice strain model fits from this work were compared to results from the published lattice strain parabola inversion code, DOUBLE FIT (Dalou et al., 2018), which parameterizes pyroxene M1 and M2 parabolas for 2+, 3+ and 4+ elements based on partition coefficients and cation radii provided by the user. It was developed for cases where elements substitute into multiple lattice sites as the HREEs do in some of the experiments in this work. This program can be run without parameter constraints, but the user may manually limit parameters to a specific range to get a better fit to their data. Without any intervention, the program produced parameters for the M2 site to a close approximation to our models (Figure S5). However, a direct comparison could not be made for the M1 site due to an elemental limitation in the DOUBLE FIT model, such that the recovered lattice strain parabola terms and fit quality were inconsistent (see caption to Figure S5 for details).

Garnet X-site parabolas were determined using the same nonlinear regression method as for the pyroxenes; reported values for D_0, E, r_0 and are presented in Table 5. The garnet X-site is assumed to have 8-fold (dodecahedral) coordination. The model fits (Figure 5d-e) show that LREE (primarily La) deviate from the parabolas defined by heavier REEs, presumably owing to larger analytical error produced by their low concentrations in the garnets (<0.01 ppm), otherwise the elements vary parabolically with ionic radius.

4.2 Origins of Partition Coefficient Variations in Fe-rich Clinopyroxene

4.2.1 *Charge Balancing Coupled Substitutions*

The experiments show that there is a positive correlation between pyroxene Al content and partition coefficients for trivalent and tetravalent elements substituting onto sites normally occupied by divalent elements (Figure 4). This suggests the importance of tetrahedral substitution of Al to balance excess charge on the pyroxene M sites, i.e., $\mathrm{Si}^{4+} + \mathrm{Ca}^{2+} \leftrightarrow \mathrm{Al}^{3+} + REE^{3+}$, as in magnesian systems (e.g., Gaetani and Grove, 1995; Lundstrom et al., 1998; Schwandt and McKay, 1998; Shearer et al., 2006). However, the Al-depleted ferrobasalt, and to a lesser extent the 50-50 mix experiments, exhibit some additional unique features including a positive Eu partitioning anomaly and relative enrichment of HREEs (Figure 3a).

4.2.2 *Eu Partitioning Anomalies*

The differing Eu partitioning anomalies among the samples are likely a direct result of the Al content. Since Eu is

Table 5. Pyroxene (M1 and M2) and garnet (X) lattice strain model parameters and uncertainty for 1 and 2 GPa experiments. Model parameter uncertainty cannot be determined with fewer than four elements in the inversions, which affects monovalent and tetravalent elements.

	Intermediate Basalt (1 GPa)	1σ	Intermediate Basalt (2 GPa)	1σ	50-50 Mix (1 GPa)	1σ	50-50 Mix (2 GPa)	1σ	Ferrobasalt (1 GPa)	1σ
M2 (1+)										
D_0	0.37				0.23		0.79		0.27	
r_0 (Å)	0.75				0.85		1.05		0.17	
E (GPa)	38.46				34.63		31.35		13.28	
M2 (2+)										
D_0	1.9	0.2			1.89	0.0001	1.89	0.002	2.09	0.004
r_0 (Å)	0.96	0.05			0.95	0.0001	0.96	0.0001	0.95	0.002
E (GPa)	192	92			180	0.03	163	0.41	188	0.92
M1 (3+)										
D_0					3.99	0.11	2.74	0.034	2.3	0.032
r_0 (Å)					0.58	0.007	0.63	0.01	0.65	0.002
E (GPa)					247	11.58	271	23.35	402	16.8
M2 (3+)										
D_0	0.16	0.15			0.07	0.001	0.12	0.001	0.03	0.001
r_0 (Å)	1	0.01			1.02	0.004	1.01	0.004	1.01	0.008
E (GPa)	193	93			233	19.32	215	15.95	186	26.92
M1 (4+)										
D_0	0.63						1.03		0.13	
r_0 (Å)	0.65						0.65		0.63	
E (GPa)	2530						4080		2414	
X (3+)										
D_0			8.5	1.39						
r_0 (Å)			0.92	0.01						
E (GPa)			515.6	89.23						

Table 5. Continued.

	Ferrobasalt (2 GPa)	1σ	Intermediate Basalt (2.5 GPa)	1σ	Intermediate Basalt (5 GPa)	1σ
M2 (1+)						
D_0	0.29					
r_0 (Å)	0.99					
E (GPa)	46.45					
M2 (2+)						
D_0	1.96	0.0004				
r_0 (Å)	0.96	0.0001				
E (GPa)	170	0.09				
M1 (3+)						
D_0	2.41	0.014				
r_0 (Å)	0.67	0.002				
E (GPa)	318	11.08				
M2 (3+)						
D_0	0.09	0.003				
r_0 (Å)	1.01	0.01				
E (GPa)	180	37.33				
X (3+)						
D_0			128.6	100	1061.30	106.48
r_0 (Å)			0.76	0.12	0.72	0.09
E (GPa)			283.2	108.52	287.2	100

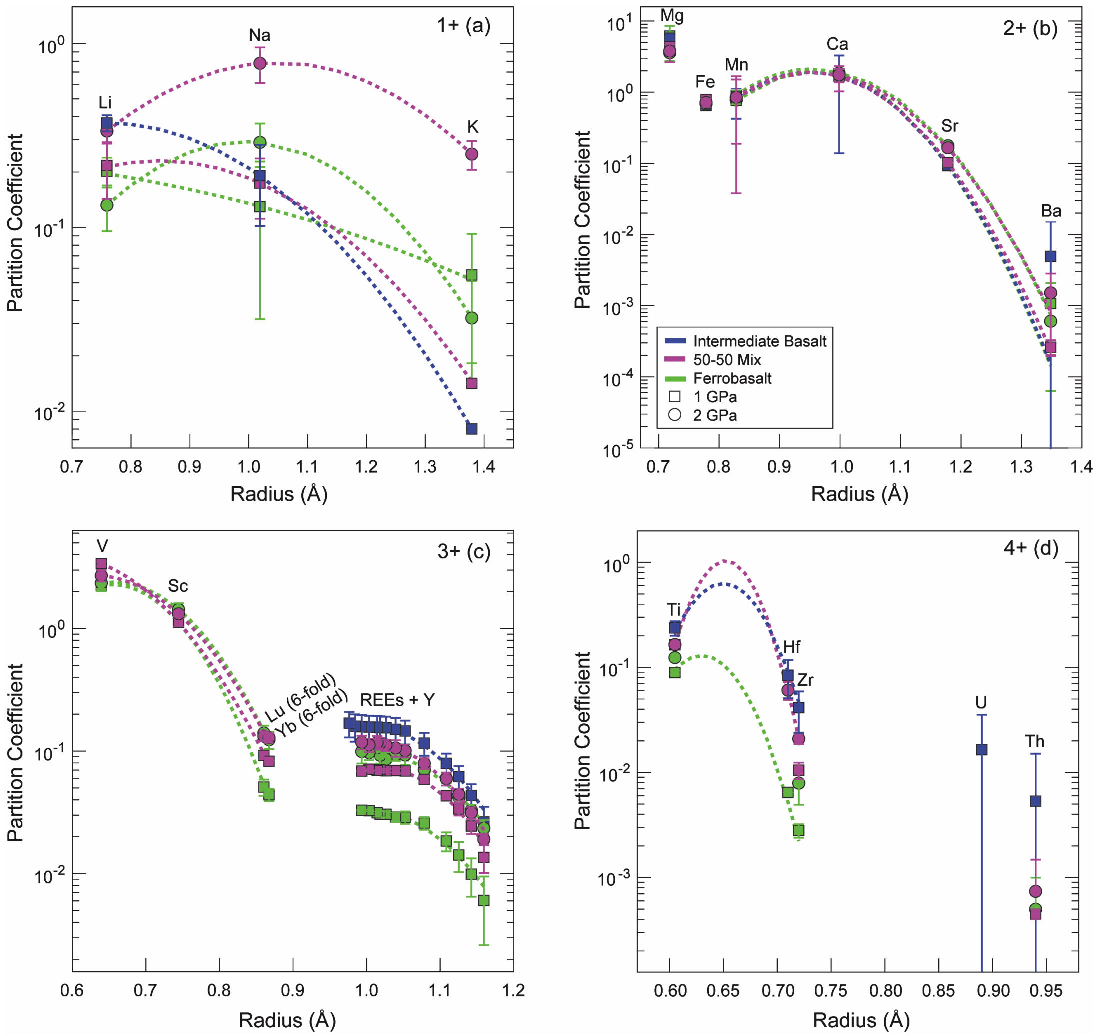

Figure 4. Lattice strain model fits to the pyroxene-melt partitioning data for 1+, 2+, 3+, and 4+ cations, and partition coefficients for 2+ and 4+ cations that do not exhibit parabolic behavior.

predominately divalent under these fO_2 conditions (~IW-1; Schreiber et al., 1987), the partitioning of the 2+ cations should be similar amongst the three compositions since they do not require a coupled substitution to charge balance the substitution. Indeed the Eu partition coefficients among the 1 GPa samples differ, 0.048 for the ferrobasalt, 0.076 for the 50-50 mix, and 0.10 for the intermediate basalt (Figure 3a). The difference among the samples that makes the Eu partitioning anomaly notable is the varying partitioning of the trivalent REEs adjacent to Eu on a spider diagram (Sm and Gd), where Sm and Gd are being directly affected by the presence (or lack thereof) of tetrahedral Al to charge balance their substitution into the structure (Figure 3a).

To determine the degree of the anomaly, the measured Eu partition coefficient (D_{Eu}) can be compared to the logarithmic interpolation of the Eu partition coefficient (D_{Eu*}):

$$D_{Eu^*} = \sqrt{D_{Sm} \times D_{Gd}} \tag{3}$$

where D_{Sm} and D_{Gd} are the measured partition coefficients for neighboring elements Sm and Gd. The values of D_{Eu}/D_{Eu*} are plotted in Figure 6 against Al_T for each experimental pyroxene. A D_{Eu}/D_{Eu*}value of one indicates no anomaly, a value greater than one is a positive anomaly and a value less than one is a negative anomaly.

The Eu anomalies vary between the 1 and 2 GPa series, where the 1 GPa series shows a systematic inverse correlation of the anomaly with the Al_T composition (Figure 6). In the 2 GPa experiments, the Eu anomaly is effectively absent (Figures 3a and 6). The 2 GPa experiments have increased Al_T content relative to their 1 GPa counterparts, consistent with previous experimental work (e.g., Thompson, 1974). Pressure, temperature and composition all contribute to determine the partitioning behavior of REE^{3+} in the clinopyroxene structure, apparently eliminating the positive Eu anomaly in the 2 GPa series.

4.2.3 HREE Partitioning Anomalies

The anomalous increase of HREE partition coefficients in the ferrobasalt (and 50-50 mix) pyroxenes may occur because of their high Fe contents (e.g., Figure 3a). The 1 GPa ferrobasalt has the lowest Mg#, approximately 9, thus the abundance of larger Fe^{2+} is greater than the slightly smaller Mg^{2+} cation (0.78 and 0.72 Å respectively in sixfold coordination, Shannon, 1976). Previous studies have argued that high concentrations of Fe and Mn in clinopyroxenes

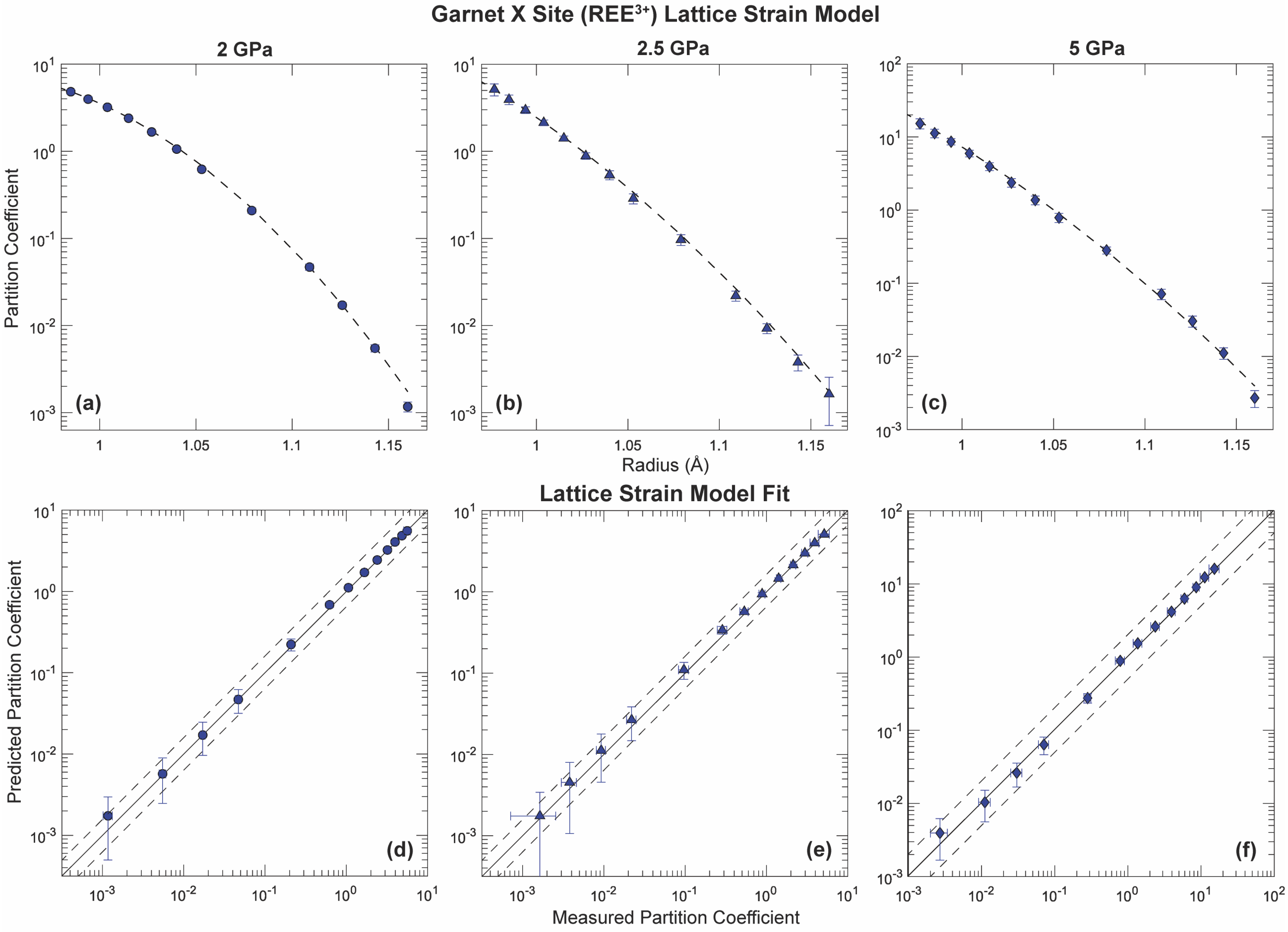

Figure 5. Lattice strain model fit for the REEs in the garnet X-site plotted with experimentally determined partition coefficients at 2 GPa (a), 2.5 GPa (b) and 5 GPa (c). Predicted versus measured partition coefficients show the fit of the model for 2 GPa (d), 2.5 GPa (e) and 5 GPa experiments (f).

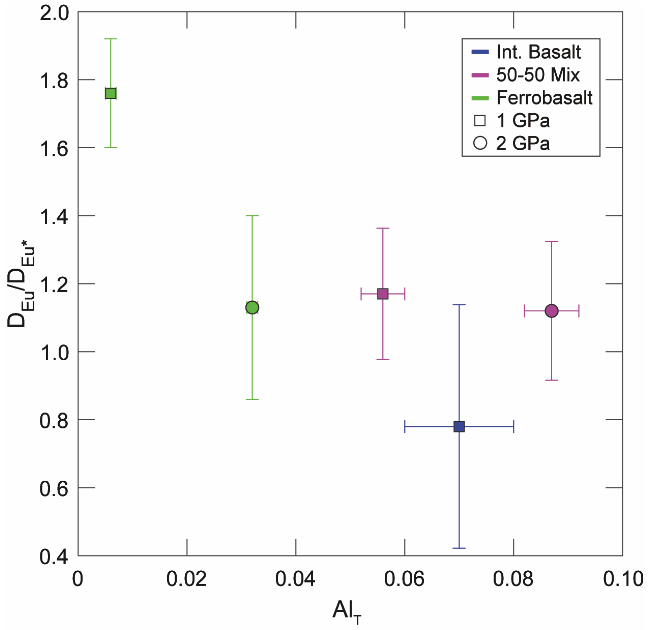

Figure 6. Eu partitioning anomaly (presented as measured D_{Eu} divided by interpolated D_{Eu*}) versus tetrahedral Al for 1 and 2 GPa pyroxene partition coefficients.

may lead to HREE partitioning in 6-fold coordination onto the M1 site (Olin and Wolff, 2010; Dygert et al., 2014; also see Rutstein and Yund, 1969 for information on lattice dimension changes with increasing Fe). To charge balance the clinopyroxene structure with a 3+ cation in the M1 site and no tetrahedral Al present, additional coupled substitutions must occur. One such mechanism is the partitioning of a monovalent cation (M^+, e.g., K^+, Na^+) into the M2 site (Harlow, 1997):

$$(Fe, \mathrm{Mg})^{2+} + \mathrm{Ca}^{2+} \leftrightarrow HREE^{3+} + M^+. \tag{4}$$

Both the ferrobasalt and the 50-50 mix pyroxenes exhibit elevated Na^+ and K^+ partition coefficients relative to the 1 GPa intermediate basalt (Figure 6a), in perhaps facilitating this type of coupled substitution.

4.2.4 Physical Controls on Partitioning Behavior

In Figure 7, lattice strain model parameter D_0 (strain free partition coefficient) for M2 2+, M2 3+, and M1 3+ from this work and from previous studies are plotted against temperature (in °C), Al_T, and and NBO/T which is the ratio of non-bridging oxygen to the number of tetrahedra in a silicate melt (a measure of the average number of oxygen shared between tetrahedral complexes). Additional lattice

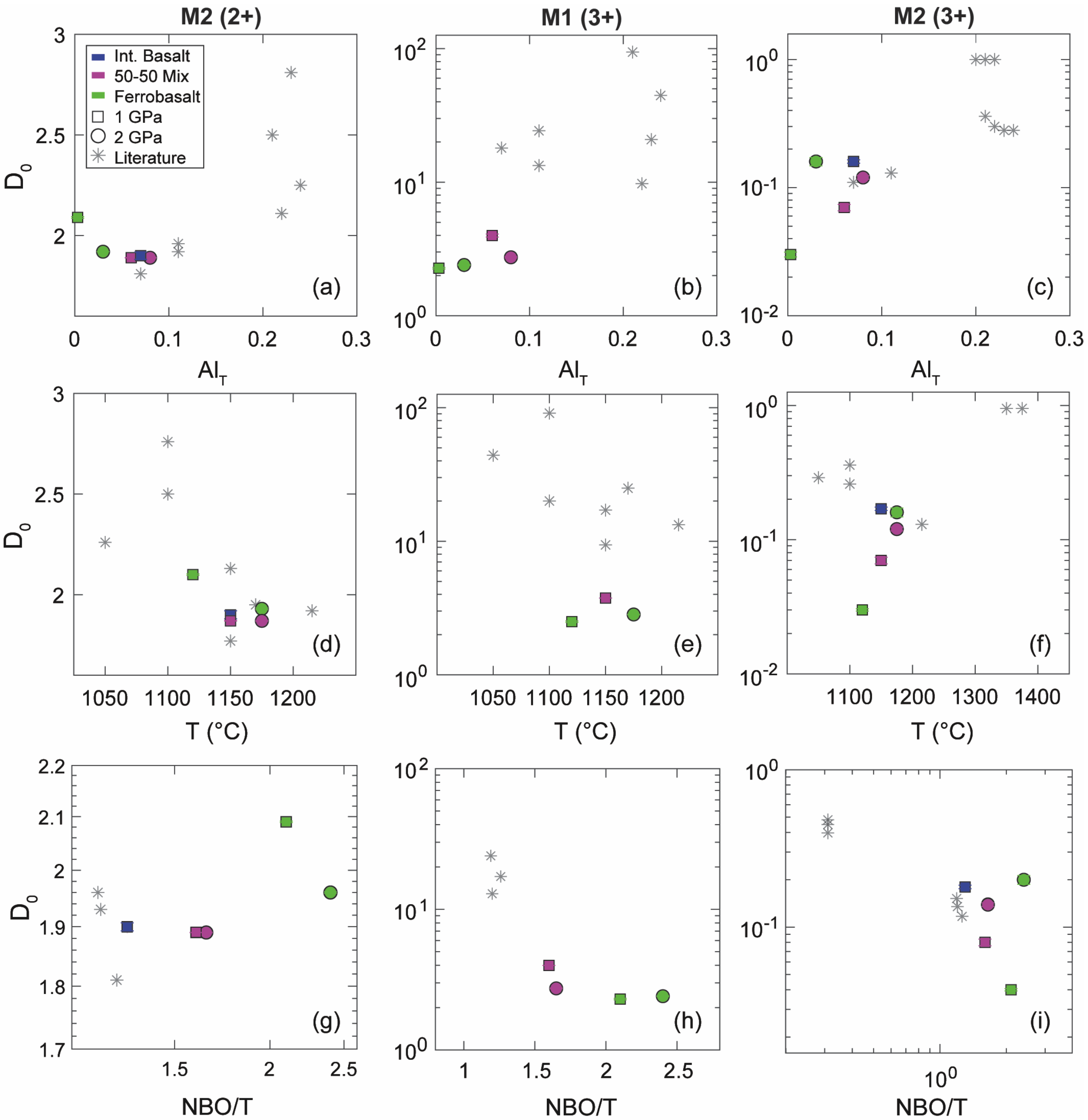

Figure 7. Pyroxene lattice strain model strain free partition coefficient (D_0) from this work and the literature (Pertermann and Hirschmann, 2002; Dygert et al., 2014, 2015) compared to (a-c) AlT, (d-f) T (°C), and (g-i) NBO/T. More figures are included in the Supplementary Material that show the correlation of E, D_0, and r_0 to Al_T, T, X_{Fe}^{M1}, and NBO/T (Figures S7-10).

strain model parameter relationships (D_0, r_0, E) compared to temperature, AlT, X_{Fe}^{M1}, and NBO/T can be found in the Supplementary Material (Figures S7-10).

Comparison of D_0 with T, NBO/T and Al_T reveals correlations of all three terms with D_0, suggesting the terms are interrelated to a certain extent. For all lattice sites, the modeled values from this work and literature show a general trend of increasing D_0 with increasing Al_T (Figure 7a-c). An inverse correlation is also apparent with NBO/T, where the lower NBO/T (more silicic compositions) correlate with higher D_0 (Figure 7 g-i). The correlation with this index of polymerization is even more dramatic with the inclusion of data from highly silicic systems (Olin and Wolff, 2010). In most cases, lower D_0 values are associated with higher temperatures (Figure 7d-e), but for the M2 3+ site, D_0 increases with increasing temperature. The relationship of X_{Fe}^{M1}on the lattice parameters are consistent within the data from this work (Figure S7), where higher D_0 is correlated to an increase in X_{Fe}^{M1} between the 1 and 2 GPa series in the 50-50 mix and ferrobasalt compositions, which is also correlated with an increase in Al_T between the samples at increasing pressure.

It makes sense that among experiments, NBO/T is correlated with T, as the degree of polymerization of a melt is related to liquidus temperature. Consequently, T or NBO/T is correlated with D_0, the other may be as well. Similarly, Al substitution into pyroxenes must be temperature dependent to some extent, such that a systematic correlation of T or

Al_T with D_0 may necessarily produce a systematic correlation with the other parameter. These covariations make it difficult to disentangle which parameters physically control partitioning behavior. Melt structure clearly has an effect on partition coefficients in highly silicic systems (Olin and Wolff, 2010), but meta-analysis of trace element partitioning data in basaltic systems suggests that T and crystal chemistry, specifically Al partitioning on the tetrahedral site, are more important in depolymerized basaltic systems (Sun and Liang, 2012). Based on the aforementioned crystal chemical arguments and our experimental observations (Figures 6 and 7), we concur with Sun and Liang (2012) and previous experimental studies from magnesian systems (Colson et al., 1989; Gallahan and Nielsen, 1992; Hauri et al., 1994; Gaetani and Grove, 1995), and suggest that in Fe-rich basaltic systems, in temperature, tetrahedral Al substitution plays a dominant role in controlling the partitioning behavior of highly charged cations in pyroxenes.

4.3 Fe- and Al-based Predictive Model for the M1 Lattice Site

Pyroxene compositions most similar to this work are from Dygert et al. (2014). In that study, the authors parameterized Fe- and Al-based predictive lattice strain models (Dygert et al., 2014, 2015) that can be used to calculate REE partition coefficients between silicate melt and the clinopyroxene M2 site as a function of temperature and composition. The published Fe- and Al-based models successfully recover the more aluminous intermediate basalt pyroxene from this study (Figure S11). However, as pyroxene composition becomes more Fe-rich and Al-depleted, the existing models overestimate the partition coefficients. Additionally, the models are incapable of recovering partition coefficients of HREEs and other trivalent elements on the M1 site. Thus, we focus here on parameterization of a predictive model for HREE and other trivalent element substitutions onto the M1 site.

Using the newly determined M1 3+ cation partition coefficients (Sc, Lu, Yb, and V; the latter is predominately 3+ at IW-1; Papike et al., 2016), from the 1 and 2 GPa ferrobasalt and 50-50 mix experiments, two experiments from Dygert et al. (2014, HB5 and HB7), a composition and temperature dependent predictive model was parameterized. The D_0 term (Eq. 2) is calculated as a function of crystal-chemical and temperature effects:

$$D_0 = -a_1 + \frac{a_2}{RT} + a_3 \times X_{Fe}^{M1} + a_4 \times X_{Al}^{T} \tag{5}$$

where X_{Fe}^{M1} is the Fe component in the M1 lattice site and X_{Al}^{T} is the tetrahedral Al component. The terms a_1, a_2, a_3, and a_4 are parameterized by nonlinear regression utilizing partition coefficients, temperature, and X_{Fe}^{M1} and X_{Al}^{T} experimental data as dependent and independent variables, respectively. E and r_0 (Eq. 2) are simultaneously inverted along with a_1-a_4.

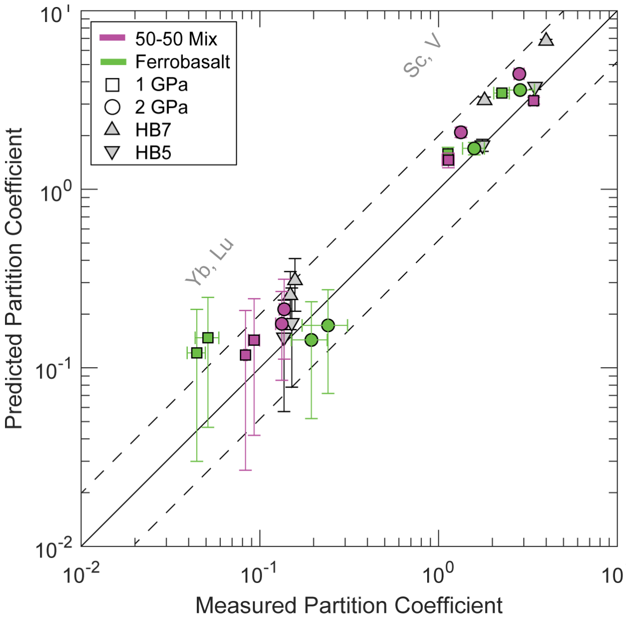

Figure 8. Fe-, Al-, and T-based model predictions for 3+ cations the M1 lattice site (Yb, Lu, Sc, V) versus the measured partition coefficients from the 1 and 2 GPa ferrobasalt and 50-50 mix experiments, and HB5 and HB7 from Dygert et al. (2014).

The resulting expressions for E, r_0, and D_0 are:

$$D_0 = -8.54(\pm 0.17) + \frac{2.76(\pm 0.01) \times 10^5}{RT} + 10.64(\pm 0.12) \times X_{Fe}^{M1} + 25.42(\pm 0.01) \times X_{Al}^{T} \tag{6}$$

$$E = 263.86(\pm 127.29) \tag{7}$$

$$r_0 = 0.62(\pm 0.01) \tag{8}$$

Uncertainty for each parameter is in parentheses (2σ). The fit quality was tested by comparing the predicted and measured partition coefficients from each experiment (Figure 8). The model recovers the experimental determinations and previously published data (HB5 and HB7, Dygert et al., 2014) to close approximation for Sc and V whereas predicted Yb and Lu partition coefficients have larger uncertainties and diverge farther from the measurements. Nonetheless, all the predictions are within uncertainty of the measured values or differ from the measurements by less than a factor of two. Parameterization of future models will benefit from further experimental characterization of HREE partitioning in the 6-fold coordinated M1 site in Fe-rich systems.

4.4 Prediction of Garnet Partition Coefficients

Published garnet-melt partitioning studies focus mainly on Mg-rich garnets (e.g., Johnson, 1998; Salters and Longhi, 1999; van Westrenen et al., 1999, 2000; Klemme et al., 2002; Salters et al., 2002; Bennett et al., 2004; Pertermann et al., 2004). An existing predictive garnet-melt partitioning model (Sun and Liang, 2013) calibrated using the magnesian partitioning data recovers measured partition coefficients

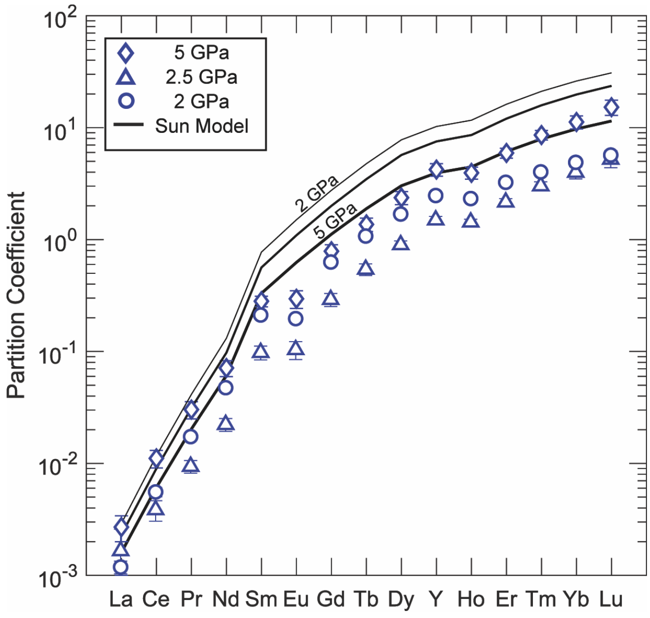

Figure 9. Measured REE partition coefficients for the intermediate basalt garnet and model predicted partition coefficients using the garnet-melt partitioning model from Sun and Liang (2013).

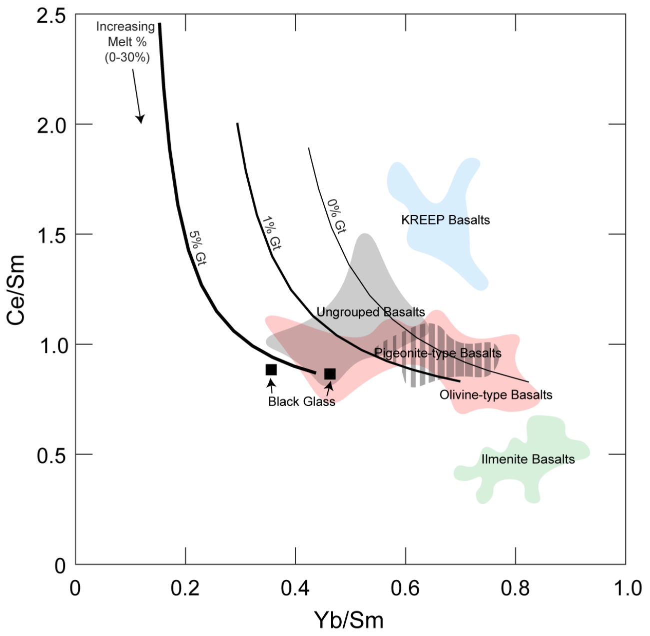

Figure 10. Batch melting models (0–30% melting) of an enriched pyroxenite source with variable amount of garnet (0–5%). Lunar basalt data were sourced from the lunar sample compendium (Meyer, 2005). Black glass data are from Shearer et al. (1990). Trace element abundances used to calculate the ratios are chondrite normalized (Anders and Grevesse, 1989).

when extrapolated to the 5 GPa experiment. However, for the lower pressure, more Fe-rich garnets, the model overestimates the HREE partition coefficients (Figure 9), presumably owing to a lack of Fe-rich garnet data in the model calibration dataset. More partitioning data from Fe-rich systems are needed to calibrate improved next-generation predictive garnet-melt partitioning models.

4.5 Application to the Petrogenesis of Lunar Basalts

To explore the potential influences of incompatible element rich pyroxenes and garnets in the lunar mantle on the compositions of lunar basalts, a modal batch melting model of a garnet-free and garnet-bearing (1–5%) pyroxenite formed after lunar magma ocean solidification was explored using the new experimentally determined partition coefficients for clinopyroxene and garnet, and reported orthopyroxene and olivine partition coefficients from literature (Dygert et al., 2020). The initial lunar mantle source composition was modeled after the Snyder et al. (1992) solidification sequence assuming a chondritic bulk Moon (Dygert et al., 2014). The mantle source considered here (in trace element compositions representing lherzolite-websterite layers from Snyder et al., 1992) included olivine, orthopyroxene, and clinopyroxene, with variable but minor amounts of garnet assumed (0–5 wt%).

The melting model results are presented in Figure 10. The Figure shows regions where different lunar basalt groups and black glasses plot relative to their Ce/Sm and Yb/Sm ratios. The ratios are useful in interpreting the relative proportions of HREE (Yb) to mid-light REE (Sm and Ce, respectively) and thereby the mineral components in the source. The use of ratios makes the results independent of the concentrations assumed in the initial bulk Moon. Increasing the garnet component results in preferential retention of HREEs during melting owing to the compatibility of HREEs in garnet, which produces lower Yb/Sm in the coexisting liquid (Figure 10). As the garnet proportion increases at any extent of melt, Ce/Sm decreases, demonstrating the greater incompatibility of Ce than Sm in garnet-bearing sources. According to chemical fractionations predicted by these models, some basalt groups (olivine-type, pigeonite-type, ungrouped) could have derived from sources containing garnet. Among the samples investigated here, those most consistent with a garnet-bearing source are black glasses, which fall close to the 5% garnet source melting, with the best fits to the data at higher extents of partial melting (Figure 10).

5 Conclusions

Fe-rich basaltic magmas are products of late-stage, or more evolved mafic systems and are common on terrestrial bodies across the Solar System, such as Mars, the Moon, and meteorite parent bodies. Trace element partitioning behavior in mafic systems is important for understanding petrogenetic processes. This work experimentally studied trace element partitioning behavior in clinopyroxenes in ferrobasaltic systems with variable Fe and Al contents, and in Fe-rich garnets, to explore how trace element partitioning differs in Fe-rich systems from magnesian systems.

Clinopyroxenes in the most aluminous experiments had the highest trivalent and tetravalent element partition coefficients and exhibited neutral or positive Eu anomalies.

Clinopyroxene in an Al-depleted, Fe-rich experiment had the lowest trivalent and tetravalent partition coefficients and exhibited a positive Eu partitioning anomaly. Collectively, the experiments reveal that much like in Mg-rich systems, Al substitution controls the partitioning of 3+ cations into the M2 site of the clinopyroxene structure via coupled substitution with tetrahedral Al, e.g., $Ca^{2+}+Si^{4+} \leftrightarrow REE^{3+}+Al^{3+}$. The change of Eu anomaly sign with Al content reflects depletion or enrichment of REE^{3+} cations according to the Al abundance. Clinopyroxenes in Fe-rich experiments exhibit anomalously higher heavy REE partition coefficients than in the more Fe-poor experiments. We interpret this as reflecting HREE partitioning onto the M1 site in 6-fold coordination, as HREEs in 6-fold coordination have ionic radii similar to Fe^{2+}. The lattice strain model was applied to the experimentally determined partition coefficients. Using the 3+ M1 lattice site partition coefficients, a new model was parameterized to predict the partitioning behavior of $HREE^{3+}$ and other trivalent elements on the M1 lattice site at different temperature conditions and as a function of clinopyroxene Al and Fe content.

In addition to clinopyroxene, experiments conducted at higher pressures (≥2 GPa) produced Fe-rich garnet, providing an opportunity to constrain garnet-melt trace element partitioning in lunar-relevant systems that have not been investigated previously. Extrapolation of an existing temperature and composition-dependent predictive partitioning model (Sun and Liang, 2013) to these garnets is moderately successful. As an application of the new partitioning data, petrogenetic models investigated the formation of lunar basalts, testing the potential role of garnet in hybridized mantle sources. Partial melting of garnet-bearing sources is consistent with some lunar basalt groups, especially the black glasses, which could have derived from a source with up to 5% garnet in the Moon's deep interior.

Acknowledgements

Thank you to Nathan Miller, Emma Bullock, and Allan Patchen for assistance with LA-ICP-MS and EPMA measurements, and to Brendan Anzures for conditioning the starting material. We are grateful for constructive comments from Handling Editor Sarah Lambart, J. Brian Balta, and one anonymous reviewer that helped improve the quality of this manuscript. Funding for this work was provided by NASA grant 80NSSC20K0467 to N.D.

6 Data, code, and outputs availability

Supporting figures, data, and codes used in the manuscript are available in the accompanying Supplementary Material and the data and software publication of Mouser (2025, https://doi.org/10.5281/zenodo.16056028). Main text figures and tables are available for download in the online version of this article.

Licence agreement

References

Anders E, Grevesse N (1989). Abundances of the elements: Meteoritic and solar. *Geochimica et Cosmochimica Acta* 53(1): 197–214. doi:10.1016/0016-7037(89)90286-x.

Barr JA, Grove TL (2013). Experimental petrology of the Apollo 15 group A green glasses: Melting primordial lunar mantle and magma ocean cumulate assimilation. *Geochimica et Cosmochimica Acta* 106: 216–230. doi:10.1016/j.gca.2012.12.035.

Baudouin C, France L, Boulanger M, Dalou C, Devidal JL (2020). Trace element partitioning between clinopyroxene and alkaline magmas: parametrization and role of M1 site on HREE enrichment in clinopyroxenes. *Contributions to Mineralogy and Petrology* 175(5). doi:10.1007/s00410-020-01680-6.

Beard BL, Taylor LA, Scherer EE, Johnson CM, Snyder GA (1998). The Source Region and Melting Mineralogy of High-Titanium and Low-Titanium Lunar Basalts Deduced from Lu-Hf Isotope Data. *Geochimica et Cosmochimica Acta* 62(3): 525–544. doi:10.1016/s0016-7037(97)00373-6.

Beard CD, van Hinsberg VJ, Stix J, Wilke M (2019). Clinopyroxene/Melt Trace Element Partitioning in Sodic Alkaline Magmas. *Journal of Petrology* 60(9): 1797–1823. doi:10.1093/petrology/egz052.

Bennett S, Blundy J, Elliott T (2004). The effect of sodium and titanium on crystal-melt partitioning of trace elements. *Geochimica et Cosmochimica Acta* 68(10): 2335–2347. doi:10.1016/j.gca.2003.11.006.

Bertka CM, Fei Y (1997). Mineralogy of the Martian interior up to core-mantle boundary pressures. *Journal of Geophysical Research: Solid Earth* 102(B3): 5251–5264. doi:10.1029/96jb03270.

Blatter DL, Sisson TW, Hankins WB (2023). Garnet stability in arc basalt, andesite, and dacite—an experimental study. *Contributions to Mineralogy and Petrology* 178(6). doi:10.1007/s00410-023-02008-w.

Blundy J, Wood B (2003). Partitioning of trace elements between crystals and melts. *Earth and Planetary Science Letters* 210(3–4): 383–397. doi:10.1016/s0012-821x(03)00129-8.

Brice J (1975). Some thermodynamic aspects of the growth of strained crystals. *Journal of Crystal Growth* 28(2): 249–253. doi:10.1016/0022-0248(75)90241-9.

Bédard JH (2014). Parameterizations of calcic clinopyroxene—Melt trace element partition coefficients. *Geochemistry, Geophysics, Geosystems* 15(2): 303–336. doi:10.1002/2013gc005112.

Cameron M, Papike J (1981). Structural and chemical variations in pyroxenes. *American Mineralogist* 66: 1–50.

Colson R, McKay G, Taylor L (1989). Charge balancing of trivalent trace elements in olivine and low-Ca pyroxene: A test using experimental partitioning data. *Geochimica et Cosmochimica Acta* 53(3): 643–648. doi:10.1016/0016-7037(89)90007-0.

Corgne A, Armstrong LS, Keshav S, Fei Y, McDonough WF, Minarik WG, Moreno K (2012). Trace element partitioning between majoritic garnet and silicate melt at 10–17 GPa: Implications for deep mantle processes. *Lithos* 148: 128–141. doi:10.1016/j.lithos.2012.06.013.

Corgne A, Wood BJ (2004). Trace element partitioning between majoritic garnet and silicate melt at 25GPa. *Physics of the Earth and Planetary Interiors* 143–144: 407–419. doi:10.1016/j.pepi.2003.08.012.

Dalou C, Boulon J, T Koga K, Dalou R, Dennen RL (2018). DOUBLE FIT: Optimization procedure applied to lattice strain model. *Computers & Geosciences* 117: 49–56. doi:10.1016/j.cageo.2018.04.013.

Deines P, Nafziger RH, Ulmer GC, Woermann E (1974). Temperature – oxygen fugacity tables for selected gas mixtures in the system C-H-O at one atmosphere total pressure. *Bulletin of the Earth and Mineral Sciences Experiment Station* 88.

Deines P, Nafziger RH, Ulmer GC, Woermann E (1976). Temperature-oxygen fugacity tables for selected gas mixtures in the system C-H-O at one atmosphere total pressure. *Metallurgical Transactions B* 7(1): 143–143. doi:10.1007/bf02652831.

Drake MJ (1975). The oxidation state of europium as an indicator of oxygen fugacity. *Geochimica et Cosmochimica Acta* 39(1): 55–64. doi:10.1016/0016-7037(75)90184-2.

Draper DS, duFrane SA, Shearer CK, Dwarzski RE, Agee CB (2006). High-pressure phase equilibria and element partitioning experiments on Apollo 15 green C picritic glass: Implications for the role of garnet in the deep lunar interior. *Geochimica et Cosmochimica Acta* 70(9): 2400–2416. doi:10.1016/j.gca.2006.01.027.

Dwarzski RE, Draper DS, Shearer CK, Agee CB (2006). Experimental insights on crystal chemistry of high-Ti garnets from garnet-melt partitioning of rare-earth and high-field-strength elements. *American Mineralogist* 91(10): 1536–1546. doi:10.2138/am.2006.2100.

Dygert N, Draper D, Rapp J, Lapen T, Fagan A, Neal C (2020). Experimental determinations of trace element partitioning between plagioclase, pigeonite, olivine, and lunar basaltic melts and an fO2 dependent model for plagioclase-melt Eu partitioning. *Geochimica et Cosmochimica Acta* 279: 258–280. doi:10.1016/j.gca.2020.03.037.

Dygert N, Liang Y, Sun C, Hess P (2014). An experimental study of trace element partitioning between augite and Fe-rich basalts. *Geochimica et Cosmochimica Acta* 132: 170–186. doi:10.1016/j.gca.2014.01.042.

Dygert N, Liang Y, Sun C, Hess P (2015). Corrigendum to ‘An experimental study of trace element partitioning between augite and Fe-rich basalts’ [Geochim. Cosmochim. Acta 132 (2014) 170–186]. *Geochimica et Cosmochimica Acta* 149: 281–283. doi:10.1016/j.gca.2014.09.013.

Gaetani GA, Grove TL (1995). Partitioning of rare earth elements between clinopyroxene and silicate melt: Crystal-chemical controls. *Geochimica et Cosmochimica Acta* 59(10): 1951–1962. doi:10.1016/0016-7037(95)00119-0.

Gallahan W, Nielsen R (1992). The partitioning of Sc, Y, and the rare earth elements between high-Ca pyroxene and natural mafic to intermediate lavas at 1 atmosphere. *Geochimica et Cosmochimica Acta* 56(6): 2387–2404. doi:10.1016/0016-7037(92)90196-p.

Harlow GE (1997). K in clinopyroxene at high pressure and temperature; an experimental study. *American Mineralogist* 82(3–4): 259–269. doi:10.2138/am-1997-3-403.

Hauri EH, Wagner TP, Grove TL (1994). Experimental and natural partitioning of Th, U, Pb and other trace elements between garnet, clinopyroxene and basaltic melts. *Chemical Geology* 117(1–4): 149–166. doi:10.1016/0009-2541(94)90126-0.

Hess P, Parmentier E (1995). A model for the thermal and chemical evolution of the Moon’s interior: implications for the onset of mare volcanism. *Earth and Planetary Science Letters* 134(3–4): 501–514. doi:10.1016/0012-821x(95)00138-3.

Hess P, Rutherford M, Campbell H (1978). Ilmenite crystallization in nonmare basalt- Genesis of KREEP and high-Ti mare basalt. In *Proceedings of the 9th Lunar and Planetary Science Conference*, vol. 1, p. 705–725.

Ji D, Dygert N (2024). Trace element partitioning between apatite and silicate melts: Effects of major element composition, temperature, and oxygen fugacity, and implications for the volatile element budget of the lunar magma ocean. *Geochimica et Cosmochimica Acta* 369: 141–159. doi:10.1016/j.gca.2023.11.004.

Jing JJ, Lin Y, Knibbe JS, van Westrenen W (2022). Garnet stability in the deep lunar mantle: Constraints on the physics and chemistry of the interior of the Moon. *Earth and Planetary Science Letters* 584: 117491. doi:10.1016/j.epsl.2022.117491.

Johnson KTM (1998). Experimental determination of partition coefficients for rare earth and high-field-strength elements between clinopyroxene, garnet, and basaltic melt at high pressures. *Contributions to Mineralogy and Petrology* 133(1–2): 60–68. doi:10.1007/s004100050437.

Kesson S, Ringwood A (1976). Mare basalt petrogenesis in a dynamic moon. *Earth and Planetary Science Letters* 30(2): 155–163. doi:10.1016/0012-821x(76)90241-7.

Klemme S, Blundy JD, Wood BJ (2002). Experimental constraints on major and trace element partitioning during partial melting of eclogite. *Geochimica et Cosmochimica Acta* 66(17): 3109–3123. doi:10.1016/s0016-7037(02)00859-1.

Li H, Zhang N, Liang Y, Wu B, Dygert NJ, Huang J, Parmentier EM (2019). Lunar Cumulate Mantle Overturn: A Model Constrained by Ilmenite Rheology. *Journal of Geophysical Research: Planets* 124(5): 1357–1378. doi:10.1029/2018je005905.

Longhi J (2003). A new view of lunar ferroan anorthosites: Postmagma ocean petrogenesis. *Journal of Geophysical Research: Planets* 108(E8). doi:10.1029/2002je001941.

Lundstrom C, Shaw H, Ryerson F, Williams Q, Gill J (1998). Crystal chemical control of clinopyroxene-melt partitioning in the Di-Ab-An system: implications for elemental fractionations in the depleted mantle. *Geochimica et Cosmochimica Acta* 62(16): 2849–2862. doi:10.1016/s0016-7037(98)00197-5.

Medard E, McCammon CA, Barr JA, Grove TL (2008). Oxygen fugacity, temperature reproducibility, and H2O contents of nominally anhydrous piston-cylinder experiments using graphite capsules. *American Mineralogist* 93(11–12): 1838–1844. doi:10.2138/am.2008.2842.

Meyer C (2005). Lunar Sample Compendium. http://curator.jsc.nasa.gov/lunar/lsc/index.cfm.

Mouser M (2025). meganmouser/PxGt-Trace-Element-Partitioning: Updated files V1.2.2. Zenodo. doi:10.5281/zenodo.16056028.

Münker C (2010). A high field strength element perspective on early lunar differentiation. *Geochimica et Cosmochimica Acta* 74(24): 7340–7361. doi:10.1016/j.gca.2010.09.021.

Neal CR (2001). Interior of the Moon: The presence of garnet in the primitive deep lunar mantle. *Journal of Geophysical Research: Planets* 106(E11): 27865–27885. doi:10.1029/2000je001386.

Neal CR, Taylor LA (1992). Petrogenesis of mare basalts: A record of lunar volcanism. *Geochimica et Cosmochimica Acta* 56(6): 2177–2211. doi:10.1016/0016-7037(92)90184-k.

Novak G, Gibbs G (1971). The Crystal Chemistry of the Silicate Garnets. *American Mineralogist* 56: 791–825.

Ohtani E (1985). The primordial terrestrial magma ocean and its implication for stratification of the mantle. *Physics of the Earth and Planetary Interiors* 38(1): 70–80. doi:10.1016/0031-9201(85)90123-2.

Olin PH, Wolff JA (2010). Rare earth and high field strength element partitioning between iron-rich clinopyroxenes and felsic liquids. *Contributions to Mineralogy and Petrology* 160(5): 761–775. doi:10.1007/s00410-010-0506-2.

Papike JJ, Hodges FN, Bence AE, Cameron M, Rhodes JM (1976). Mare basalts: Crystal chemistry, mineralogy, and petrology. *Reviews of Geophysics* 14(4): 475–540. doi:10.1029/rg014i004p00475.

Papike JJ, Simon SB, Burger PV, Bell AS, Shearer CK, Karner JM (2016). Chromium, vanadium, and titanium valence systematics in Solar System pyroxene as a recorder of oxygen fugacity, planetary provenance, and processes. *American Mineralogist* 101(4): 907–918. doi:10.2138/am-2016-5507.

Pertermann M, Hirschmann MM (2002). Trace-element partitioning between vacancy-rich eclogitic clinopyroxene and silicate melt. *American Mineralogist* 87(10): 1365–1376. doi:10.2138/am-2002-1012.

Pertermann M, Hirschmann MM, Hametner K, Günther D, Schmidt MW (2004). Experimental determination of trace element partitioning between garnet and silica-rich liquid during anhydrous partial melting of MORB-like eclogite. *Geochemistry, Geophysics, Geosystems* 5(5). doi:10.1029/2003gc000638.

Rutstein M, Yund R (1969). Unit-cell parameters of synthetic diopside-hedenbergite solid solutions. *American Mineralogist* 54: 238–245.

Salters VJ, Longhi J (1999). Trace element partitioning during the initial stages of melting beneath mid-ocean ridges. *Earth and Planetary Science Letters* 166(1–2): 15–30. doi:10.1016/s0012-821x(98)00271-4.

Salters VJM, Longhi JE, Bizimis M (2002). Near mantle solidus trace element partitioning at pressures up to 3.4 GPa. *Geochemistry, Geophysics, Geosystems* 3(7): 1–23. doi:10.1029/2001gc000148.

Schreiber HD, Merkel RC, Schreiber VL, Balazs GB (1987). Mutual interactions of redox couples via electron exchange in silicate melts: Models for geochemical melt systems. *Journal of Geophysical Research: Solid Earth* 92(B9): 9233–9245. doi:10.1029/jb092ib09p09233.

Schwandt CS, McKay GA (1998). Rare earth element partition coefficients from enstatite/melt synthesis experiments. *Geochimica et Cosmochimica Acta* 62(16): 2845–2848. doi:10.1016/s0016-7037(98)00233-6.

Shannon RD (1976). Revised effective ionic radii and systematic studies of interatomic distances in halides and chalcogenides. *Acta Crystallographica Section A* 32(5): 751–767. doi:10.1107/s0567739476001551.

Shearer C, Papike J (1993). Basaltic magmatism on the Moon: A perspective from volcanic picritic glass beads. *Geochimica et Cosmochimica Acta* 57(19): 4785–4812. doi:10.1016/0016-7037(93)90200-g.

Shearer C, Papike J, Galbreath K, Shimizu N (1991). Exploring the lunar mantle with secondary ion mass spectrometry: a comparison of lunar picritic glass beads from the Apollo 14 and Apollo 17 sites. *Earth and Planetary Science Letters* 102(2): 134–147. doi:10.1016/0012-821x(91)90003-z.

Shearer C, Papike J, Karner J (2006). Pyroxene europium valence oxybarometer: Effects of pyroxene composition, melt composition, and crystallization kinetics. *American Mineralogist* 91(10): 1565–1573. doi:10.2138/am.2006.2098.

Shearer C, Papike J, Simon S, Shimizu N, Yurimoto H, Sueno S (1990). Ion microprobe studies of trace elements in Apollo 14 volcanic glass beads: Comparisons to Apollo 14 mare basalts and petrogenesis of picritic magmas. *Geochimica et Cosmochimica Acta* 54(3): 851–867. doi:10.1016/0016-7037(90)90378-x.

Shearer CK, Papike JJ (1999). Magmatic evolution of the Moon. *American Mineralogist* 84(10): 1469–1494. doi:10.2138/am-1999-1001.

Snape JF, Nemchin AA, Johnson T, Luginbühl S, Berndt J, Klemme S, Morrissey LJ, van Westrenen W (2022). Experimental constraints on the long-lived radiogenic isotope evolution of the Moon. *Geochimica et Cosmochimica Acta* 326: 119–148. doi:10.1016/j.gca.2022.04.008.

Snyder GA, Taylor LA, Neal CR (1992). A chemical model for generating the sources of mare basalts: Combined equilibrium and fractional crystallization of the lunar magmasphere. *Geochimica et Cosmochimica Acta* 56(10): 3809–3823. doi:10.1016/0016-7037(92)90172-f.

Sun C, Graff M, Liang Y (2017). Trace element partitioning between plagioclase and silicate melt: The importance of temperature and plagioclase composition, with implications for terrestrial and lunar magmatism. *Geochimica et Cosmochimica Acta* 206: 273–295. doi:10.1016/j.gca.2017.03.003.

Sun C, Liang Y (2012). Distribution of REE between clinopyroxene and basaltic melt along a mantle adiabat: effects of major element composition, water, and temperature. *Contributions to Mineralogy and Petrology* 163(5): 807–823. doi:10.1007/s00410-011-0700-x.

Sun C, Liang Y (2013). The importance of crystal chemistry on REE partitioning between mantle minerals (garnet, clinopyroxene, orthopyroxene, and olivine) and basaltic melts. *Chemical Geology* 358: 23–36. doi:10.1016/j.chemgeo.2013.08.045.

Suzuki T, Hirata T, Yokoyama TD, Imai T, Takahashi E (2012). Pressure effect on element partitioning between minerals and silicate melt: Melting experiments on basalt up to 20GPa. *Physics of the Earth and Planetary Interiors* 208–209: 59–73. doi:10.1016/j.pepi.2012.07.008.

Thompson RN (1974). Some high-pressure pyroxenes. *Mineralogical Magazine* 39(307): 768–787. doi:10.1180/minmag.1974.039.307.04.

Tual L, Smit MA, Kooijman E, Kielman-Schmitt M, Ratschbacher L (2022). Garnet, zircon, and monazite age and REE signatures in (ultra)high-temperature and high-pressure rocks: Examples from the Caledonides and the Pamir. *Journal of Metamorphic Geology* 40(8): 1321–1346. doi:10.1111/jmg.12667.

Tuff J, Gibson SA (2007). Trace-element partitioning between garnet, clinopyroxene and Fe-rich picritic melts at 3 to 7 GPa. *Contributions to Mineralogy and Petrology* 153(4): 369–387. doi:10.1007/s00410-006-0152-x.

Unruh DM, Stille P, Patchett PJ, Tatsumoto M (1984). Lu-Hf and Sm-Nd evolution in lunar mare basalts. *Journal of Geophysical Research: Solid Earth* 89(S02). doi:10.1029/jb089is02p0b459.

Wadhwa M (2008). Redox Conditions on Small Bodies, the Moon and Mars. *Reviews in Mineralogy and Geochemistry* 68(1): 493–510. doi:10.2138/rmg.2008.68.17.

Walker D, Longhi J, Stolper EM, Grove TL, Hays JF (1975). Origin of titaniferous lunar basalts. *Geochimica et Cosmochimica Acta* 39(9): 1219–1235. doi:10.1016/0016-7037(75)90129-5.

Walter M, Nakamura E, Trønnes R, Frost D (2004). Experimental constraints on crystallization differentiation in a deep magma ocean. *Geochimica et Cosmochimica Acta* 68(20): 4267–4284. doi:10.1016/j.gca.2004.03.014.

Warren PH (1985). THE MAGMA OCEAN CONCEPT AND LUNAR EVOLUTION. *Annual Review of Earth and Planetary Sciences* 13(1): 201–240. doi:10.1146/annurev.ea.13.050185.001221.

van Westrenen W, Blundy J, Wood B (1999). Crystal-chemical controls on trace element partitioning between garnet and anhydrous silicate melt. *American Mineralogist* 84: 838–847. doi:10.2138/am-1999-5-618.

van Westrenen W, Blundy JD, Wood BJ (2000). Effect of Fe2+ on garnet–melt trace element partitioning: experiments in FCMAS and quantification of crystal-chemical controls in natural systems. *Lithos* 53(3–4): 189–201. doi:10.1016/s0024-4937(00)00024-4.

van Westrenen W, Blundy JD, Wood BJ (2001). High field strength element/rare earth element fractionation during partial melting in the presence of garnet: Implications for identification of mantle heterogeneities. *Geochemistry, Geophysics, Geosystems* 2(7). doi:10.1029/2000gc000133.

Wood MC, Gréaux S, Kono Y, Kakizawa S, Ishikawa Y, Inoué S, Kuwahara H, Higo Y, Tsujino N, Irifune T (2024). Sound velocities in lunar mantle aggregates at simultaneous high pressures and temperatures: Implications for the presence of garnet in the deep lunar interior. *Earth and Planetary Science Letters* 641: 118792. doi:10.1016/j.epsl.2024.118792.

Yu S, Tosi N, Schwinger S, Maurice M, Breuer D, Xiao L (2019). Overturn of Ilmenite-Bearing Cumulates in a Rheologically Weak Lunar Mantle. *Journal of Geophysical Research: Planets* 124(2): 418–436. doi:10.1029/2018je005739.

Yurimoto H, Ohtani E (1992). Element partitioning between majorite and liquid: A secondary ion mass spectrometric study. *Geophysical Research Letters* 19(1): 17–20. doi:10.1029/91gl02824.

Zhang N, Dygert N, Liang Y, Parmentier EM (2017). The effect of ilmenite viscosity on the dynamics and evolution of an overturned lunar cumulate mantle. *Geophysical Research Letters* 44(13): 6543–6552. doi:10.1002/2017gl073702.